Advanced Steel Construction – Vol. 19 No. 1 (2023) 23–30
DOI:10.18057/IJASC.2023.19.1.4
(**Special Issue:** *10th International Conference on Advances in Steel Structures, ICASS'2020, Chengdu, China*)

A PRELIMINARY STUDY OF DEPOSITION RATE, MATERIAL PROPERTY AND STABILITY OF WAAM STAINLESS STEEL PLATES

Siân I. Evans and Jie Wang *

Department of Architecture and Civil Engineering, University of Bath, Bath, BA2 7AY United Kingdowm
** (Corresponding author: E-mail: j.wang@bath.ac.uk)*

ABSTRACT

Wire arc additive manufacturing (WAAM) has significant potential to produce freeform, but structurally efficient geometries out of stainless steel, for use in the construction industry, however, there is currently no standardisation of the manufacturing parameters used to produce WAAM structures. This paper discusses an experimental programme carried out on WAAM 316L stainless steel plated structures to assess the effects of the deposition rate, which is directly associated with productivity. This programme comprises tensile tests on coupons extracted along different printing directions, geometric imperfection measurement (including surface roughness, waviness and overall out-of-straightness), and stub column tests designed to determine the local stability of unstiffened plates manufactured with different deposition rates. The applicability of current Eurocode design rules for stainless steel structures, including the ductility requirements and effective width equations, have been assessed based on the obtained experimental data.

ARTICLE HISTORY

Received: 20 July 2022
Revised: 22 August 2022
Accepted: 10 January 2023

KEYWORDS

Wire arc additive manufacturing (WAAM);
Advanced steel construction;
3D printing;
Local buckling;
Material proterties;
Unstiffened plates

1. Introduction

The construction industry accounts for 30% of the world's greenhouse gas emissions, 30% of raw material use worldwide, and 36% of global energy usage [1] and so it is under a lot of pressure to become more sustainable. Improving material utilization through use of additive manufacturing (AM) may help to achieve this. Large metal structures are required in the construction industry and wire arc additive manufacturing (WAAM, a form of direct energy deposition) has the capability to produce these [2] at a viable rate of production due to its rapid deposition rate [1]. Unfortunately, this rapid deposition rate may compromise the surface quality and dimensional accuracy of the part [3] and introduce further potential defects including high residual stress, distortion, porosity and anisotropic material properties [4].

Numerous variables can be adjusted to alter the properties of the build, including the deposition rate, the heat input, the interpass temperature, and the direction of the build. It is not yet fully understood how these variables affect the structural response of WAAM builds. The only experiments [5]–[7] currently available that have investigated the overall structural stability performance of WAAM structures have been carried out on specimens produced with invariant and manufacturer-determined parameters.

Previous material tests on WAAM builds have given inconsistent results, with some authors finding that the Young's modulus (E) of machined samples was higher for those extracted at 45° to the substrate, than for those extracted at 0° or 90° [6], [8], whilst others have found no significant differences in E across samples extracted from different angles [9]. Previous literature also indicates that E is generally 20% less for as-built samples than machined samples due to their undulating geometry [10]. The ultimate tensile strength (σ_u) has been found to be highest at 45° to the substrate because this is where there is the highest density of cell boundaries along the main slip direction [9], and it has been found to be lowest at 90° to the substrate because here the part is loaded across its layers [6].

This paper aims to detail the results from a series of experiments undertaken to assess the effects of the deposition rate and the build direction on key material properties, geometric accuracy and structural stability. The experiments comprise tensile coupon tests, stub column tests and geometric imperfection measurements on 316L stainless steel parts made by WAAM. 316L stainless steel was chosen because it has high strength, high ductility, relatively low cost, and excellent corrosion resistance [4]. The applicability of current Eurocode design rules for stainless steel structures, including the ductility requirements and effective width equation have been assessed based on the obtained test data.

2. Sample fabrication

2.1. WAAM rig and selecting printing parameters

All samples for these experiments have been manufactured on a WAAM rig comprised of an ESAB Aristo 4004i pulse system welding power supply (in MIG set up), a three-axis cartesian motion system (comprised of three servo-drives), an extractor, an enclosure, an Omron controller, and a computer to program the rig on (Fig. 1). The welding torch is located on the Z-axis and is controlled using motion instructions sent using Trajexia software.

The builds employed a wire diameter of 0.8 mm to ensure a thin weld bead was produced. The wire feed speed (WFS) also affects the thickness of a build so a suitable range of 8-10 m/min was chosen to again ensure that slender parts could be manufactured. These combinations of wire diameter and WFS led to a high deposition rate of 2.42 kg/hr and a low deposition rate of 1.93 kg/hr. The specimens produced using these two deposition rates were denoted with 'H' (high deposition) and 'L' (low deposition), respectively.

The control manufacturing parameters used were a heat input of 0.415 kJ/mm, an interpass temperature of 150°C, the welding technology (MIG), the shield gas flow rate and composition, the contact tip distance (7 mm), the feedstock (0.8 mm diameter 316L stainless steel wire), the substrate design and fixture, and the motion system. The voltages used were 29.2 V for the H-specimens and 29.0 V L-specimens because the voltage varies slightly with WFS. A heat input of 0.415 kJ/mm was chosen as it gave stable bead geometry. In order to achieve this heat input, the travel speed was 10.313 mm/s and 12.917 mm/s for the L-specimens and H-specimens, respectively.

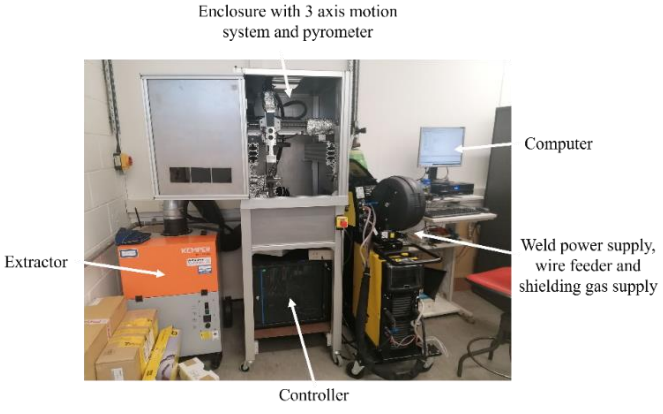

Fig. 1 Labelled photograph of the rig

2.2. Fabrication and preparation of tensile coupons

The coupons were extracted from two plates (each 150 mm wide by 100 mm tall, with a nominal thickness of 3 mm) produced using the two different deposition rates (2.42 kg/hr and 1.93 kg/hr), which were denoted as PH and PL (Plate with High (or Low) deposition rate), respectively. The plates were made in layers on 50×200×6 mm 316L stainless steel substrates. Each layer was deposited, before the height of the welding torch was updated manually on the welding program, with the increase in height being measured using a Vernier calliper. This process was repeated until the plates were 100 mm tall.

Once PH and PL were produced, they were sawn from the substrates (reducing the height of each plate to approximately 80 mm), and six coupons were cut from each plate by water jetting cutting. The dimensions of the coupons are based on the sub-size rectangular specimens specified in the ASTM E8/E8M-13 [11] and were scaled down by a ratio of 0.75:1 to ensure the coupons would fit on the plate. This scaling allowed the gauge length-to-width ratio to remain at 4, required by this standard. The coupons were extracted at different angles to the build direction, as shown in Fig.2b, with the spacing between coupons being flexible. Unfortunately, only one coupon could be extracted from each plate at 0° to the substrate due to constraints on the size of the plates.

Each tensile coupon is named using the following convention: TH or TL (depending on if the coupon is from PH or PL) – angle to the substrate – coupon number as indicated in Fig.2b. After extraction, the coupons were machined to a nominal thickness of 2 mm (or 1.6 mm where the surface waviness required this) to ensure a uniform thickness across their lengths. TL-90-3 had a surface waviness too great for it to be machined flat, so it was not tested.

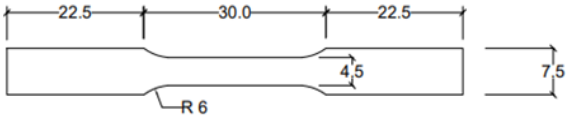

(a) Coupon dimensions

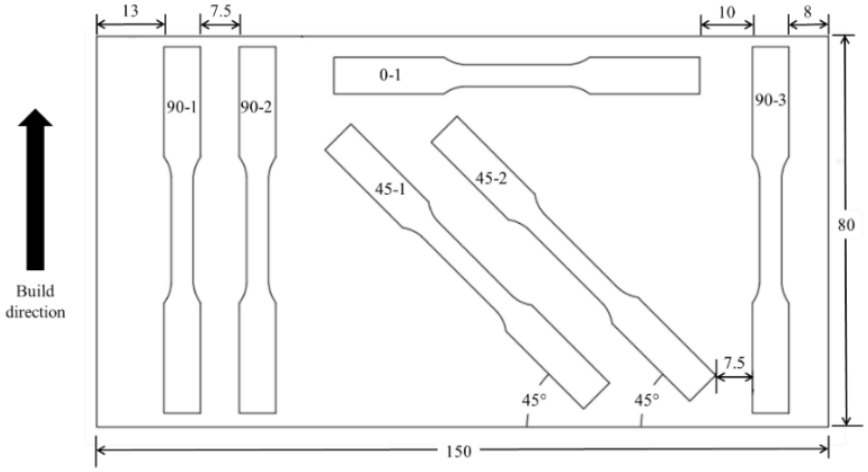

(b) Coupon locations on plate (mm)

Fig. 2 Tensile coupon dimensions and locations

2.3. Fabrication and preparation of EAS stub columns

Four equal angle section (EAS) stub columns were manufactured, with two using the higher deposition rate (labelled as EH1 and EH2), and two using the lower deposition rate (labelled as EL1 and EL2). The substrates used were 75×100×6 mm and the EAS had nominal dimensions Width×Width×Height of 50×50×100 mm. The fabrication of these EAS stub columns followed the same process as the corresponding PL or PH specimens, with the samples being built such that they are compressed in the 90° direction during testing.

Once built, the samples were sawn off the substrates and large welding drops caused by balling were roughly removed from the surface, preventing their noise on the measured geometries while ensuring that the waviness and roughness remained (Fig. 3). Next, the ends were hand filed to be parallel with each other and perpendicular to the longitudinal direction. They were then sanded with wet and dry paper, before being lapped with lapping paste to ensure that the load would be distributed across the entire cross-section of each column from the very beginning of the compression tests.

Fig. 3 The stub column samples after being removed from the substrates and with balling roughly removed (from left to right, samples EL1, EL2, EH1 and EH2)

3. Tensile tests and results

The coupons were tested at room temperature using an Instron 3369 50 kN testing frame which measured the load, and an 8 mm clip gauge extensometer to measure the strain. Displacement control (calculated from the estimated strain rates over the parallel length required in EN ISO 6892-1 [12] ($\leq$0.00007 s^{-1} in the elastic range and $\leq$0.00024 s^{-1} in the plastic range)) was used. There was no clearly defined yield point for any of the tests, so the strain rate was changed when it was clear that the stress-strain graph had started to curve. This occurred at displacements between 0.75 mm and 1.5 mm depending on sample.

Despite all surface undulations being removed before testing, the coupons exhibited surface deformations which corresponded to their building directions (as shown in Fig. 4). This has previously been found by other authors as well [8].

Fig. 4 The sample TH-45-2 after testing. It has been placed back together and there are surface deformations visible at 45° to the length of the coupon, corresponding to the fact that the coupon was extracted from the WAAM build at 45°.

The obtained stress-strain curves are shown in Fig. 5 and the key material properties including the Young's modulus (E), the 0.2% proof stress ($\sigma_{0.2}$), the ultimate tensile strength (σ_u), the strain at ultimate tensile strength (ε_u), the percentage elongation after fracture (ε_f) measured according to [12], and strain hardening parameters n and m (from the modified O-R model [13]) are given in Table 1. These are compared to benchmark values for conventionally produced 316L stainless steel in Fig. 6 and an assessment of the ductility of each sample is shown in Fig. 7.

Samples extracted from the same plate and at the same angle were expected to have similar E, however, E for sample TH-45-2 is 22.1% less than that of sample TH-45-1. Similarly, coupon TH-90-3 has a much lower E than samples TH-90-1 and TH-90-2. This variation could indicate that E varies across the build, however, there is not yet enough data to conclude this. The greatest E is found for coupons extracted at 45° for both plates, whilst the E at 0° and 90° are on average 40.3% and 46.4% less than the average benchmark value respectively [14]. Both of these points reinforce findings by in [6], where E for machined samples taken at 0° or 90° were lower than conventionally produced material by about 30-55%. All samples have E below the benchmark values, indicating that WAAM samples are less stiff than traditionally produced parts.

WAAM parts are expected to have a lower failure strain when compared to wrought and annealed counterparts because internal defects and surface roughness act as stress locations and the fine microstructure makes the part less ductile as dislocation motion is limited [15]. Only three coupons had ε_f values greater than the lower benchmark value [16], which shows an agreement with this hypothesis.

All samples have $\sigma_{0.2}$ greater than the benchmark average and all coupons except TH-0-1 have σ_u values between the upper and lower benchmark values [16], indicating that WAAM is capable of producing parts of equal strength to those produced by conventional methods, but not necessarily demonstrating the increase in strength expected from the fine grains [15]. As only one coupon was extracted at 0° for each plate, this result is likely accidental. The greatest σ_u is seen at 90° for both plates, however, it is expected to be greatest at 45° [9] and lowest at 90° [6].

The three ductility requirements stated in EN 1993-1-1 [17] are all met by all coupons tested (Fig. 7), suggesting that WAAM is capable of producing parts which have acceptable ductility. It should be noted that four samples (TH-90-1, TH-90-2, TH-45-1 and TH-45-2) failed outside of the clip gauge so the strains measured from the onset of necking may be inaccurate. This could be why the former three samples all appeared to report low strains at failure.

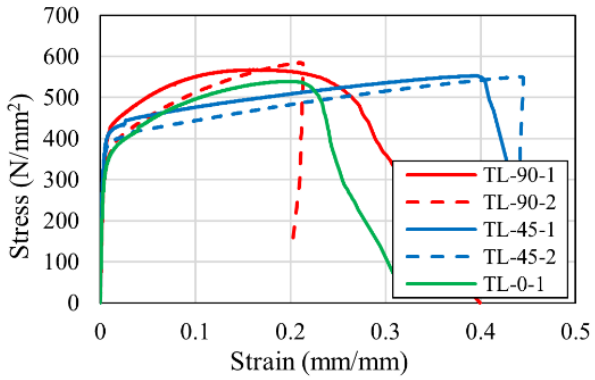

(a) Lower deposition rate

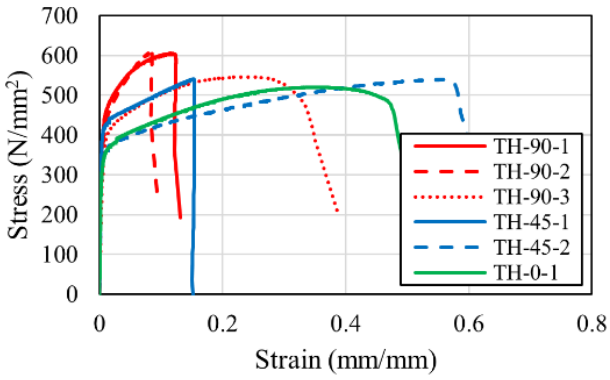

(b) Higher deposition rate

Fig. 5 The stress-strain relationships of tensile coupons

Table 1
Results of tensile coupon tests

Sample	E (N/mm²)	$\sigma_{0.2}$ (N/mm²)	σ_u (N/mm²)	ε_u (mm/mm)	ε_f (mm/mm)	n	m
TL-90-1	107436	370	567	0.165	0.318	6.05	3.28
TL-90-2	103559	313	586	0.209	0.271	7.64	2.87
TL-45-1	155854	361	553	0.393	0.391	4.43	3.27
TL-45-2	182207	338	550	0.441	0.438	2.55	3.15
TL-0-1	112008	308	539	0.197	0.340	6.73	3.00
TH-90-1	122627	395	605	0.118	0.267	6.95	3.29
TH-90-2	116825	360	610	0.084	0.203	5.67	3.07
TH-90-3	78808	324	546	0.240	0.353	5.48	3.08
TH-45-1	180844	381	541	0.152	0.269	5.72	3.47
TH-45-2	140918	325	539	0.558	0.567	4.06	3.11
TH-0-1	123797	311	520	0.353	0.473	6.95	3.10

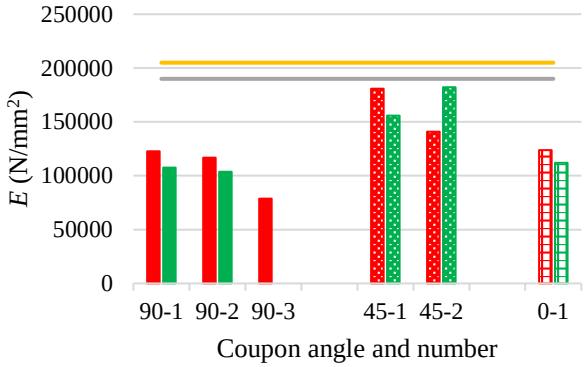

(a) Young's modulus

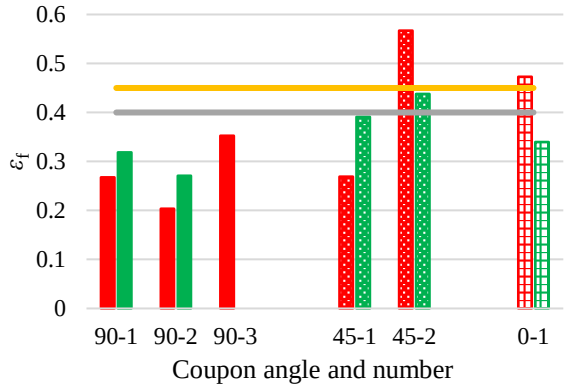

(b) percentage elongation after fracture

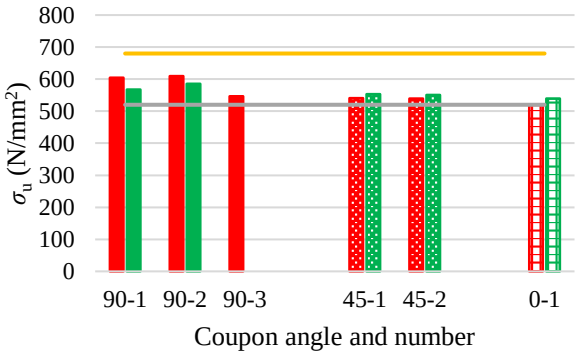

(c) Ultimate tensile strength

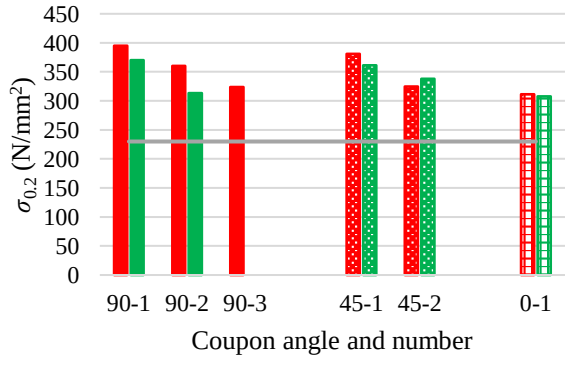

(d) 0.2% proof strength

Fig. 6 Comparison of material properties of each tensile coupon, categorised by deposition rate and angle of extraction

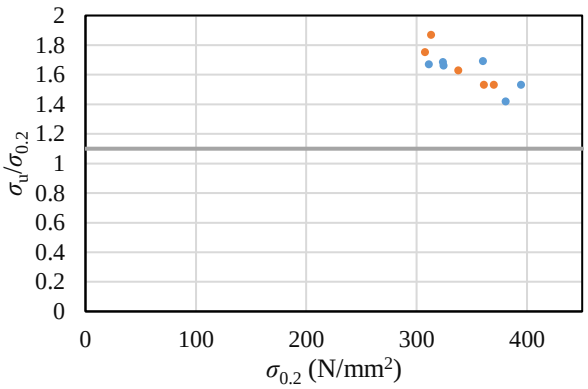

(a) Ultimate to yield strengh ratio

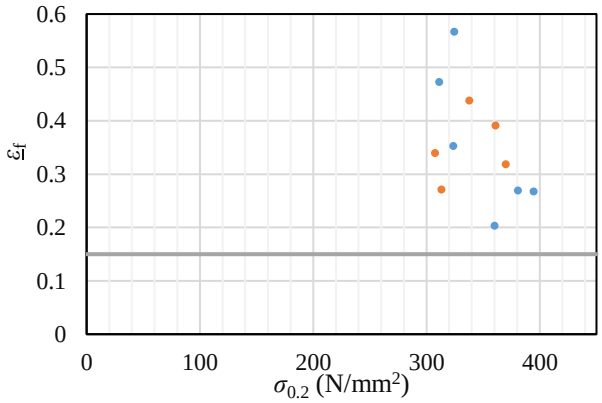

(b) Fracture strain

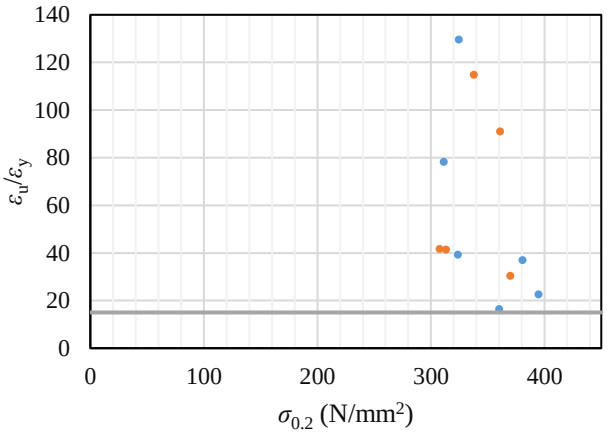

(c) Ultimate to yield strain ratio

Fig. 7 The ductility requirements [17] and results from the tensile coupon tests

4. Geometric imperfection measurement

All four stub columns were 3D scanned using a Hexagon CMS 108AP laser line scanner (30 μm accuracy), attached to a Hexagon ROMER arm, and the data was outputted to SpatialAnalyzer as point clouds. These point clouds were then analysed using MATLAB. The use of Archimedes' Principle was not deemed necessary to obtain the volume of each sample as this can be found using the results of the 3D scans, and other researchers have found the values calculated from each of these methods to be essentially identical [10].

It was observed that for all the samples, the cross-section varies across the height and width of the build, as shown in Fig. 8. Based on the obtained geometric data clouds, the average flange thickness (t_{av}), minimum thickness (t_{min}), average of minimum thicknesses between layers ($t_{av,min}$), average cross-sectional area (A_{av}), part height (L), maximum deviation of the mid-thickness from the average mid-thickness (γ), average layer height (h_{av}), slenderness ($\bar{\lambda}_p$), surface waviness (ω) (Eq. (1), where $t_{av,max}$ is the average of maximum thickness of each layer), and surface roughness S_a (Eq. (2) where f_n is the height of a peak or depth of a valley, measured at N locations), were calculated and are reported in

Table. The values for surface waviness and surface roughness were similar for all columns, so the deposition rate had no clear effect here. It was expected the EH1 and EH2 would be thicker as they were made employing a faster WFS [18], however, the measured data revealed that EL1 and EL2 have a larger minimum and average thickness than EH1 and EH2. The location of the minimum thickness varies for each column and for each flange of each column, as does the location of maximum deviation from the central line.

$$\omega = \frac{t_{av,max} - t_{av,min}}{2} \quad (1)$$

$$S_a = \frac{1}{N}\sum_{n=1}^{N}|f_n| \quad (2)$$

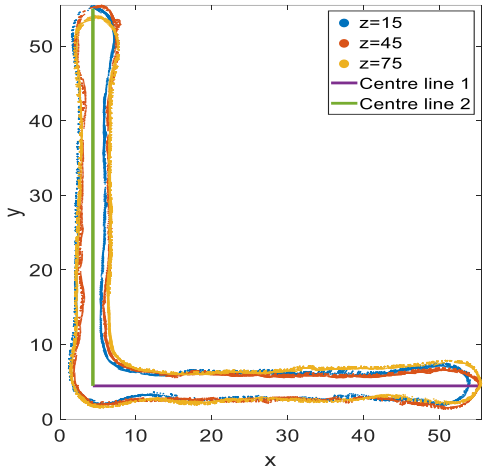

(a) Across different heights

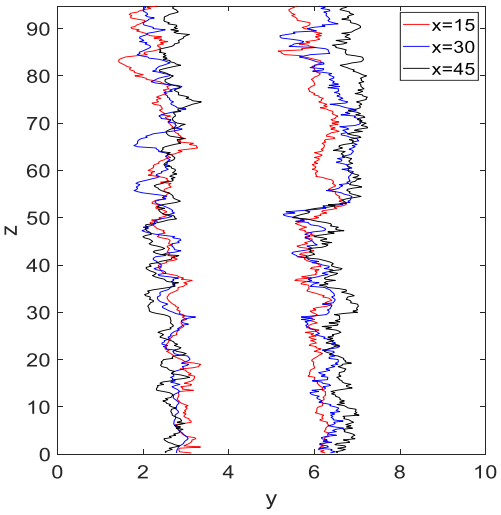

(b) Across different widths

Fig. 8 Variation in the cross-section of sample EL2 across a) different heights, and b) different widths. All units are in mm

Table 2
Measurements and material properties of the stub columns

Sample	t_{av} (mm)	t_{min} (mm)	$t_{av,min}$ (mm)	A_{av} (mm^2)	L (mm)	γ (mm)	h_{av} (mm)	ω (mm)	S_a (mm)	N_u (kN)	k_{theo} (kN/mm)	k (kN/mm)	δ_u (mm)
EL1	4.15	2.29	3.68	418	94.7	1.83	2.38	0.28	0.57	98.9	466	106	4.52
EL2	3.63	2.00	3.38	414	97.6	1.88	2.57	0.27	0.34	92.1	448	60	4.50
EH1	3.40	1.40	2.93	389	95.8	2.39	2.46	0.37	0.50	80.8	431	93	4.45
EH2	3.61	1.58	2.99	383	99.1	1.92	2.61	0.30	0.40	96.7	410	114	4.04

5. Stub column tests

5.1. Testing procedure

The tests on EAS stub columns were carried out to evaluate the stability performance of external plated elements (with only one longitudinal edge supported) manufactured by WAAM. The stub column tests were conducted on a 2000 kN loading machine, with a 9 mm thick end plate placed on top of each sample to ensure equal distribution of the applied compressive stresses. Four vertical LVDTs were set up between the upper and lower plates, along with two horizontal LVDTs on the inside faces of the EASs at approximately mid-height and mid-width (Fig. 9) to monitor the lateral displacements of the flanges. In previous work by other authors, the horizontal LVDTs have been positioned at the geometric centre of the EASs [19], however, the geometry of these EASs is imperfect so here they are placed at the centre of each flange instead.

The load was applied to each sample using displacement control (0.15 mm/min), with the load being read directly from the loading machine and the displacements being read from the LVDTs (at 0.5 Hz). Testing was concluded when a clear decline in axial load had occurred, and excessive end shortening had been observed, in line with the experimental procedures chosen by other authors [20].

5.2. Test results

The failure modes of the tested EAS stub columns are displayed in Fig. 10. It can be seen that the EL2, EH1 and EH2 stub columns all displayed a single wave of flange buckling occurring at the same height on the two flanges; however, this height was different for each column and did not necessarily occur at the mid-height. The EL1 stub column displayed two buckling waves along the length, which is very unlikely to happen in traditional rolled EAS members with "near-perfectly" flat geometries [19]. This may be caused by the manufactured imperfection, where a clear thickness offset was presented towards the upper half of the EL1 stub column, as can be seen in Fig. 3.

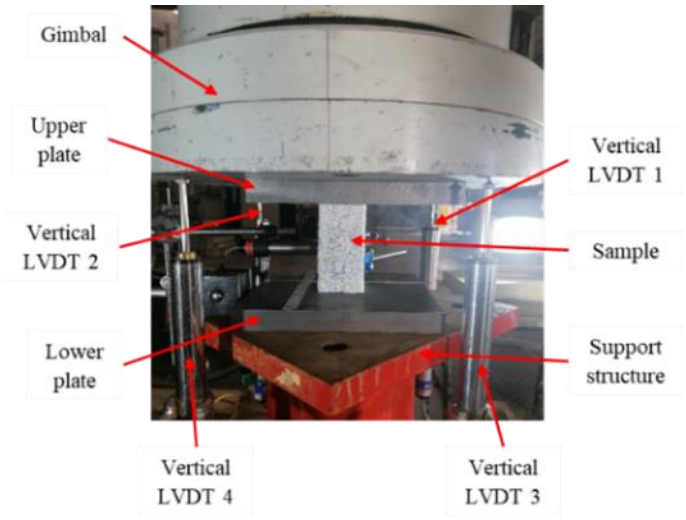

(a) Photograph of the stub column test setup

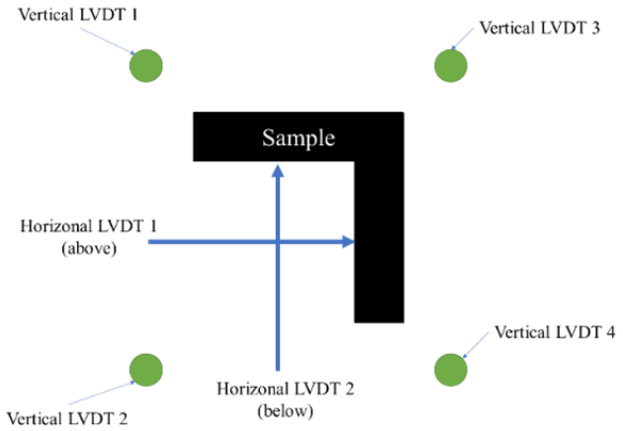

(b) Schematic plan view of the test setup

Fig. 9 a) Photograph of the setup of the LVDTs, plates and supporting structure, and b) schematic of the LVDT setup

The ultimate load (N_u), stiffness (k), and the end shortening (δ_u) of each stub column are shown in Table 1. The theoretical stiffness, k_{theo}, calculated based on the averaged cross-sectional area is also included in Table 2 for comparison purposes. For each stub column, the experimental stiffness, k, was between 13-28% of the predicted stiffness and this can be attributed to the undulating geometry of the builds and the consequence that the stiffness may not be uniform across the height of each sample. Moreover, the axial stiffness of EH specimens was expected to be less than that of EL specimens as EH specimens report greater averaged thicknesses and cross-sectional areas Table 2. However, the opposite is observed in this study, as shown in Fig. 11a where axial load vs end shortening curves of the stub columns are plotted. Therefore, predicting the stiffness using the average cross-sectional area may not be an appropriate approach and the deformability, stability and other stiffness related structural behaviour of WAAM plates needs to be carefully assessed. Further investigation may be carried out to explain this observation.

Fig. 11b shows the horizontal displacements measured during the test on EH1, with one flange buckling outward and one inward (as seen in Fig. 10). Similar results were found for the other stub columns, except for EL1 (Fig. 11c). Here, the horizontal displacements at the measured locations show that both flanges moved inwards in the initial loading stage. This may be cause by the higher order (two-buckling wave) mode of failure developed in this specimen and the measurements close to the mid-height location were not necessarily representative.

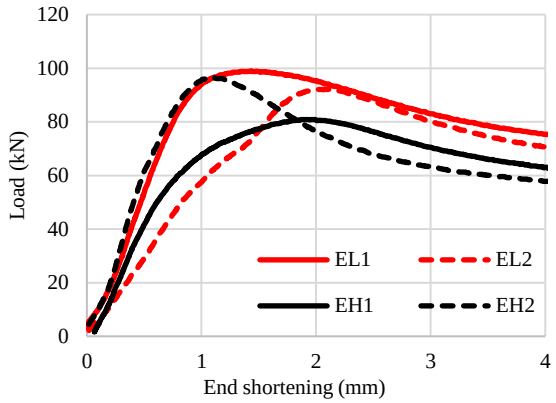

(a) Load vs end-shortening curves

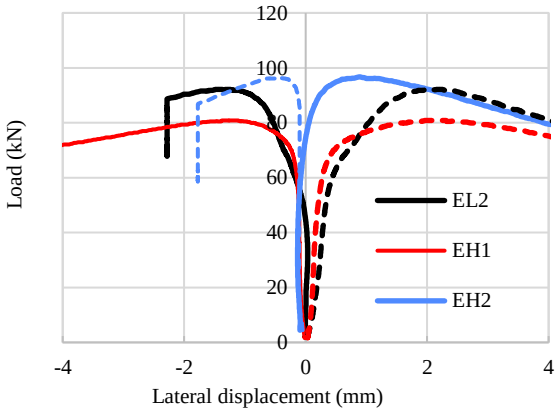

(b) Load vs lateral displacement at mid height of flanges of EL2, EH1 and EH2 stub columns

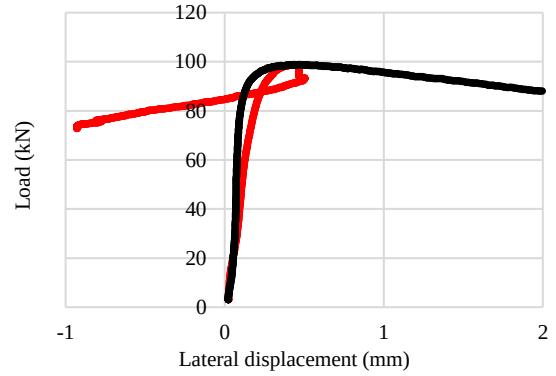

(c) Load vs lateral displacement at mid height of flanges of EL1

Fig. 11 Load displacement curves from stub column tests

Fig. 10 The buckled stub columns after testing (from left to right, samples EL1, EL2, EH1 and EH2)

5.3. Applicability of effective width equation

The buckling resistance of each column is compared with the Eurocode prediction [21] for external plate elements in Fig. 12. In Fig. 12, the vertical axis is the ultimate load N_u normalised by the plastic load $N_y = A\sigma_{0.2}$ (where A is the cross-sectional area calculated using t_{av} or $t_{av,min)}$ of each cross-section, and the horizontal axis is the average plate slenderness $\bar{\lambda}_p$ of the flanges of the EAS stub columns. The equation deriving $\bar{\lambda}_p$ is given in Eq. (3), where c is the entire flange width, t is t_{av} or $t_{av,min}$, $\varepsilon = [(235/\sigma_{0.2})(E/210000)]^{0.5}$ (with $\sigma_{0.2}$ and E based on the measured properties from the machined tensile coupons in the 90° direction), and k_σ is the buckling coefficient. k_σ = 1.3 as obtained according to the aspect ratio and boundary condition of the flange of the EAS stub columns [22]. Based on the $\bar{\lambda}_p$ values, all the samples are classified as Class 4 [17].

$$\bar{\lambda}_p = \frac{c/t}{28.4\varepsilon\sqrt{k_\sigma}} \quad (3)$$

The comparison in Fig. 12 shows that the tested samples presented significantly lower buckling resistances (calculated using t_{av}) compared to the codified prediction. However, the results calculated using $t_{av,min}$ are much closer to the prediction, suggesting that this may be a more appropriate measurement to use. Selecting the most appropriate dimensions to use in predictions of behaviour is an important issue for WAAM steel structures due to their non-uniform thickness across both the cross-section and the height. Based on the results presented in this study, it is clear that the averaged cross-sectional dimensions are not the best parameters to be used to estimate the structural performance of WAAM builds. More representative geometric parameters are sought, and a standardisation of this step is needed, which would require a large data pool and should be determined in conjunction with any modification of the local buckling equation to produce a reliable prediction of the stability performance of WAAM structures.

Another point to consider is that the properties of the stub column may be different to those of a larger column because heat accumulation may cause the top and bottom to have different microstructures. The geometry may also vary more substantially from the ideal EAS as geometric errors in printing add up, so the applicability of these results to larger columns must be considered carefully.

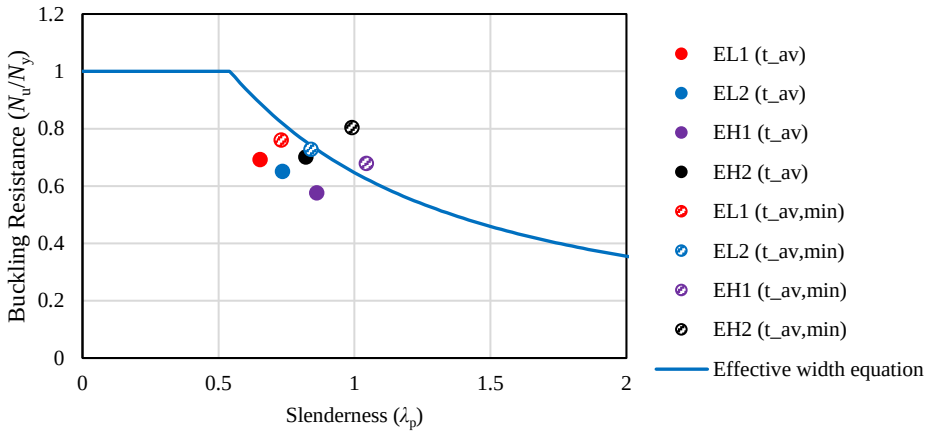

Fig. 12 The buckling resistances of each stub column (ultimate load from stub column tests/yield load from tensile coupon tests), plotted against their slenderness (calculated using t_{av} or $t_{av,min}$) along with the effective width equation [21]

6. Conclusions

This paper has investigated the effect of the deposition rate and build direction on the material, geometric and stability performance of 316L stainless steel plated structures made by WAAM. The following conclusions have been identified:

1. The Young's moduli of the tensile coupons extracted at 45° to the substrate were found to be the greatest, indicating that this direction of the build is stiffest.
2. Although the failure strain of the WAAM parts was found to be less than those of wrought and annealed parts, all tensile coupons meet the ductility requirements stated in EN 1993-1-1 [17].
3. The deposition rate was found to have no effect on the surface roughness or surface waviness. However, a lower deposition rate was found to be associated with thicker builds.
4. The buckling modes of the EAS stub columns made by WAAM were different from those of traditionally rolled steel angle sections, as can be attributed to the combined effect of their high out-of-straightness and surface waviness.
5. The average thickness and average cross-sectional area may not be the best parameters to characterize the local buckling resistance of WAAM plates under compression. Instead, the average value of the minimum thickness for each layer of the builds was found to present a better characterization of their stability performance, resulting in predictions close to the effective width equation given in EN 1993-1-4 [21]. However, a standardization of this step will require a large experimental data pool.

References

[1] C. Buchanan and L. Gardner, 'Metal 3D printing in construction: A review of methods, research, applications, opportunities and challenges', *Engineering Structures*, no. 180, pp. 332–348, Feb. 2019.

[2] S. W. Williams, F. Martina, A. C. Addison, J. Ding, G. Pardal, and P. Colegrove, 'Wire + Arc Additive Manufacturing', *Materials Science and Technology*, vol. 32, no. 7, pp. 641–647, May 2016, doi: 10.1179/1743284715Y.0000000073.

[3] Q. Wu, Z. Ma, G. Chen, C. Liu, D. Ma, and S. Ma, 'Obtaining fine microstructure and unsupported overhangs by low heat input pulse arc additive manufacturing', *Journal of Manufacturing Processes*, no. 27, pp. 198–206, 2017.

[4] C. R. Cunningham, J. Wang, V. Dhokia, A. Shrokani, and S. T. Newman, 'Characterisation of Austenitic 316LSi Stainless Steel Produced by Wire Arc Additively Manufacturing with Interlayer Cooling', presented at the Solid Freeform Fabrication 2019, Austin, USA, 2019.

[5] V. Laghi, M. Palermo, G. Gasparini, V. Girelli, and T. Trombetti, 'Experimental results for structural design of Wire-and-Arc Additive Manufactured stainless steel members', *Journal of Constructional Steel Research*, vol. 167, 2020, [Online]. Available: https://doi.org/10.1016/j.jcsr.2019.105858

[6] C. Buchanan, W. Wing, and L. Gardner, 'Testing of Wire and Arc Additively Manufactured Stainless Steel Material and Cross-Sections', Hong Kong, China, Dec. 2018.

[7] P. Kyvelou, C. Huang, L. Gardner, and C. Buchanan, 'Structural Testing and Design of Wire Arc Additively Manufactured Square Hollow Sections', *Journal of Structural Engineering*, vol. 147, no. 12, 2021.

[8] P. Kyvelou *et al.*, 'Mechanical and microstructural testing of wire and arc additively manufactured sheet material', *Materials & Design*, no. 192, p. 108675, 2020.

[9] V. Laghi, M. Palermo, L. Tonelli, G. Gasparini, L. Ceschini, and T. Trombetti, 'Tensile properties and microstructural features of 304L austenitic stainless steel produced by wire-and-arc additive manufacturing', *The International Journal of Advanced Manufacturing Technology*, no. 106, pp. 3693–3705, 2020.

[10] L. Gardner, P. Kyvelou, G. Herbert, and C. Buchanan, 'Testing and initial verification of the world's first metal 3D printed bridge', *Journal of Constructional Steel Research*, no. 172, p. 106233, 2020.

[11] ASTM International, 'ASTM E8/E8M-13, Standard Test Methods for Tension Testing of Metallic Materials'. 2013.

[12] BS EN ISO 6892, 'BS EN ISO 6892-1:2019 Metallic materials, tensile testing, method of test at room temperature'. 2020.

[13] P. Hradil, A. Talja, E. Real, E. Mirambell, and B. Rossi, 'Generalized multistage mechanical model for nonlinear metallic materials', *Thin-Walled Structures*, vol. 63, pp. 63–69, Feb. 2013, doi: 10.1016/j.tws.2012.10.006.

[14] 'Properties: Stainless Steel - Grade 316 (UNS S31600)', *AZoM.com*. https://www.azom.com/properties.aspx?ArticleID=863 (accessed Apr. 27, 2021).

[15] D. Bourell *et al.*, 'Materials for additive manufacturing', *CIRP Annals - Manufacturing Technology*, no. 66, pp. 659–681, 2017.

[16] BS EN 10088-2, 'BS EN 10088-2:2014 Stainless Steels Part 2: Technical delivery conditions for sheet/plate and strip of corrosion resisting steels for general purposes'. 2014.
[17] European Committee for Standardization (CEN), 'Eurocode 3: Design on steel structures. Part 1-1: General rules and rules for buildings', Brussels, Belgium, EN 1993-1-1:2005/A1:2014, 2015.
[18] M. Dinovitzer, X. Chen, J. Laliberte, X. Huang, and H. Frei, 'Effect of wire and arc additive manufacturing (WAAM) process parameters on bead geometry and microstructure', *Additive Manufacturing*, vol. 26, pp. 138–146, Mar. 2019.
[19] G. Shi, Z. Liu, H. Y. Ban, Y. Zhang, Y. J. Shi, and Y. Q. Wang, 'Tests and finite element analysis on the local buckling of 420 MPa steel equal angle columns under axial compression', *Steel and Composite Structures*, vol. 12, no. 1, pp. 31–51, 2011.
[20] H. X. Yuan, Y. Q. Wang, Y. J. Shi, and L. Gardner, 'Stub column tests on stainless steel built-up sections', *Thin-Walled Structures*, vol. 83, pp. 103–114, Oct. 2014.
[21] European Committee for Standardization (CEN), 'Eurocode 3: Design of steel structures. Part 1-4: General rules - Supplementary rules for stainless steels', Brussels, Belgium, EN 1993-1-4, 2006.
[22] N. S. Trahair, M. A. Bradford, D. A. Nethercot, and L. Gardner, *The Behaviour and Design of Steel Structures to EC3*, Fourth. 2008.